This is the Pre-Published Version.

This document is the Accepted Manuscript version of a Published Work that appeared in final form in ACS nano, copyright © 2019 American Chemical Society after peer review and technical editing by the publisher. To access the final edited and published work see https://doi.org/10.1021/acsnano.9b04956.

Valence Engineering *via* Dual-Cation and Boron Doping in Pyrite Selenide for Highly Efficient Oxygen Evolution

Yunpeng Zuo[†a,d], *Dewei Rao*[†b], *Sainan Ma*[†a], *Tingting Li*[c], *Yuen Hong Tsang*[a], *Stepan Kment*[d], *and Yang Chai*[*a]

[†]These authors contributed equally to this work.

[a] Department of Applied Physics, The Hong Kong Polytechnic University, Hung Hom, Kowloon, Hong Kong, P. R. China.

[b] School of Materials Science and Engineering, Jiangsu University, Zhenjiang 212013, PR China.

[c] Institute of Surface Micro and Nano Materials, Xuchang University, Xuchang, Henan 461002, PR China.

[d] Regional Centre of Advanced Technologies and Materials, Faculty of Science, Palacký University Olomouc

[*] Corresponding author. ychai@polyu.edu.hk

ABSTRACT

Valence engineering has been proved as an effective approach to modify the electronic property of catalyst and boost its oxygen evolution reaction (OER) activity, while the limited number of elements restricts the structural diversity and the active sites. Also, the catalyst performance and stability are greatly limited by cationic dissolution, ripening or crystal migration in catalytic system. Here we employed a widely used technique to fabricate heteroepitaxial pyrite selenide through dual-cation substitution and boron dopant to achieve better activity and stability. The overpotential of Ni-pyrite selenide catalyst is decreased from 543 mV to 279.8 mV at 10 mA cm^{-2} with the Tafel slope from 161 mV dec^{-1} to 59.5 mV dec^{-1}. Our theoretical calculations suggest both cation and boron doping can effectively optimize adsorption energy of OER intermediates, promote the charge transfer among the heteroatoms, and improve their OER property. This work underscores the importance of modulating surface electronic structure with the use of multiple elements, and provides a general guidance on the minimization of activity loss with valence engineering.

KEYWORDS: oxygen evolution reaction, valence engineering, pyrite selenide, multimetallic compound, boron doping

The oxygen evolution reaction (OER) has been extensively studied for the development of the sustainable and clean energy devices, such as, hydrogen fuel cells, metal-air batteries, *etc.*[1-8] The OER is based on a four electron-proton coupled reaction, requiring a high overpotential (η) with respect to the standard reduction potential $E \approx 1.23$ V.[3-6] To reduce the overpotential and the overall energy consumption of water electrolysis, researchers have developed various electrocatalytic systems to facilitate water splitting reactions.[9-25] Transition metal pyrite selenides have been demonstrated as a promising catalyst for OER, which can provide a high activity and high cost-effectiveness compared to commonly used noble metals or oxides catalysts.[8-12] However, their performances achieved so far is still rather low for practical applications.

The cation doping has been demonstrated to be an attractive approach to improve the OER activity of pyrite selenides, as it can improve the electrical conductivity and introduce more lattice vacancies as active centers.[25-28] For example Li *et al.* found out that Fe, Co dual-cation in $NiSe_2$ can enhance the Tafel slope from 105 mV dec^{-1} to 63 mV dec^{-1} for OER due to the increase of the surface active sites.[26] Song *et al.* reported crystalline-amorphous phase F-Co_2B exhibiting superior overpotential of $\approx$ 320 mV, which was better than Co_2B and RuO_2.[28] Although the interaction between the multiple element atoms can give rise to new geometries and/or surface electronic structures, the detrimental phenomena including cationic dissolution, ripening or crystal migration still limit practical applications of multimetallic selenides.[10, 25, 26]

Modifying the local electronic structure of the multimetallic selenides by valence engineering is an effective method to improve their catalytic activity and stability. As a typical valence engineering route, the favorable heteroepitaxial structure has been extensively employed to suppress ripening or crystal migration compared to single-component metal and metallic alloys.[21-25] Additionally, the boron dopant within the multimetallic selenides may relief the cationic dissolution.[16,19,20] Furthermore, the nanoscale selenides with multiple exposed sites enable the decrease of the kinetic energy barriers of the OER reaction.[20-25] The wet chemical approaches have been adopted to synthesize selenides with heterostructures at nanoscale by undergoing nucleation growth based on preformed seed particles.[22,24,30-32] The alloy composition obtained by wet chemical method is usually restricted by three elements, which greatly limits the structural diversity and the possibility of adjusting the composition.[2] Although some techniques such as printing methods, melt processing, high temperature thermal reduction combined with cold-rolling operation, have been successfully used to prepare multi-metal composites consisting of five or more elements,[31-36] these methods require sophisticated instruments, and are especially inapplicable for mixing elements with varied physical and chemical properties. In this work, we develop a facile method to produce boron dopant ternary pyrite selenide on amorphous membrane. The resulting materials exhibit superior performance in terms of low overpotential and long electrochemical stability. Our theoretical studies suggest that the boron dopant and binary atomic substitution can weaken the interaction between catalyst and OER intermediates, which enable efficient catalytic process.

RESULTS AND DISCUSSION

The boron dopant ternary pyrite selenide ($Fe_5Co_4Ni_{20}Se_{36}B_x$) was synthesized by wet chemical method. Scheme S1 depicts the growth process of $Fe_5Co_4Ni_{20}Se_{36}B_x$ nanocatalyst supported on amorphous FeCoNi-B membrane. Figure S1 shows the pre-loaded amorphous multimetallic boride membrane (MBM) selenized in a tube furnace under the nitrogen flow.

The Fe/Co/Ni/Se composition was determined to be 5:4:20:36 by using transmission electron microscopy energy-dispersive X-ray spectroscopy (TEM-EDX) and the corresponding elemental maps are displayed in Figure S2. The gaseous Se atoms react with the MBM and generate $Fe_5Co_4Ni_{20}Se_{36}B_x$ nuclei on the surface of MBM during this initial stage. The nucleus grow into small $Fe_5Co_4Ni_{20}Se_{36}B_x$ clusters with the deposition of the newly formed selenide atoms. Finally, $Fe_5Co_4Ni_{20}Se_{36}B_x$ nanoparticles were synthesized on MBM.

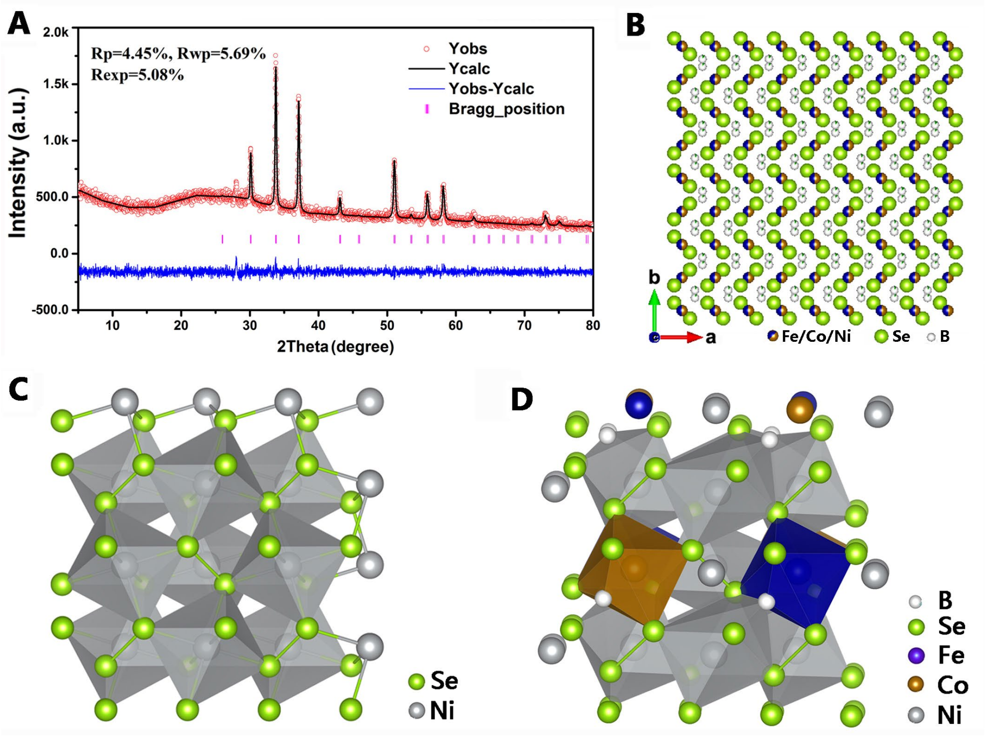

Figure 1. (A) XRD rietveld refinement of Fe5Co4Ni20Se36Bx and (B) the atomistic model; (C, D) Schematic illustration of NiSe2 and Fe5Co4Ni20Se36Bx crystal structures.

The X-ray powder diffraction (XRD) analysis was used to further understand the crystal structural of the $Fe_5Co_4Ni_{20}Se_{36}B_x$ nanoparticles. The diffraction peaks in the XRD spectrum (Figure S3) can be well identified to the (210), (200), (211), (311) and (321) for the $Fe_5Co_4Ni_{20}Se_{36}B_x$ nanomaterials compared to $NiSe_2$ with the JCPDS number 88-1711.[24-27] The Rietveld refinement analysis was carried out using the computer software General Structure Analysis System (GSAS) showing that Fe, Co and Ni atoms co-occupy in the same site with the composition ratio of 2:1 and 1:1 for Ni/(Fe+Co) and Fe/Co (Figure 1A), respectively.[37,38] These refined results reveal that B atoms are embedded in the interstitial sites of crystal. Some of them form the B-M (M=Fe, Co, Ni) bonds, as show in Figure 1B-D, while other portions bond to Se.[11,14]

The structure of $Fe_5Co_4Ni_{20}Se_{36}B_x$ materials was characterized by spherical aberration corrected transmission electron microscope (AC-TEM). The as-prepared $Fe_5Co_4Ni_{20}Se_{36}B_x$ nanoparticles are supported on the FeCoNiB membrane with good dispersion and narrow distribution of particle size (Figure 2A). The selected area electron diffraction (SAED) pattern of $Fe_5Co_4Ni_{20}Se_{36}B_x$ nanoparticles exhibits (Figure 2B) discrete and bright diffraction dots, indicating their good crystallinity.[23] The inset fast Fourier transformation (FFT) image in Figure 2C indicates the amorphous structure of the supporting membrane.[14,19] The HAADF-STEM-electron energy-loss spectroscopy (EELS) mapping was used to characterize the elemental distribution of $Fe_5Co_4Ni_{20}Se_{36}B_x$ nanoparticles (Figure 2D, E), in which the particular atoms are visualized as Fe (red), Ni (green), Co (pink), B (yellow), Se (blue). The individual elemental maps and their combined distribution map confirm the presence of all the five elements in the nanoparticles.

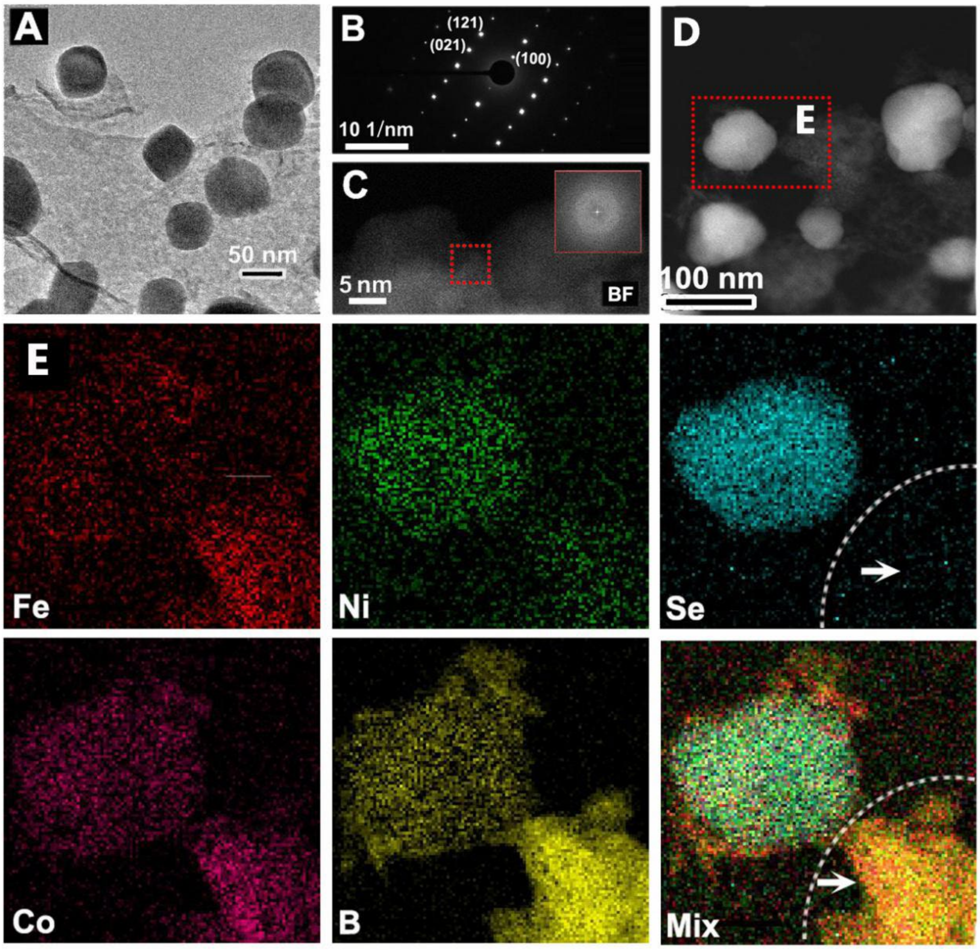

Figure 2. (A) HRTEM image and (B) SAED pattern of the $Fe_5Co_4Ni_{20}Se_{36}B_x$ nanoparticles; (C) The STEM images of the supporting membrane. The inset is the fast Fourier transformation (FFT) image; (D) STEM image of the $FeCoNiSeB_x$ catalyst and (E) the corresponding HAADF-STEM-electron energy-loss spectroscopy (EELS) mapping images.

As widely accepted, the surface structure of catalysts plays a very important role in the catalytic reaction.[15,21] Therefore, the understanding the exterior structure of catalyst is indispensable for the OER catalytic mechanism.[34-36] The atomic-resolution TEM images of $Fe_5Co_4Ni_{20}Se_{36}B_x$ nanoparticles (Figure 3) show the exposed (210) and (111) facets (Figure 3A$_1$-A$_3$, Figure 3B$_1$-B$_3$, respectively) with the corresponding FFT images, revealing the uniformity of the crystal structure. Although it is difficult to observe the exactly atomic structure through TEM images (Figure 3C, E), the corresponding simulated images in Figure

3D, F with the typical [210] and [111] zone axis reveal that the B atoms locate at interstitial sites consistent with the rietveld refinement analysis conclusions.

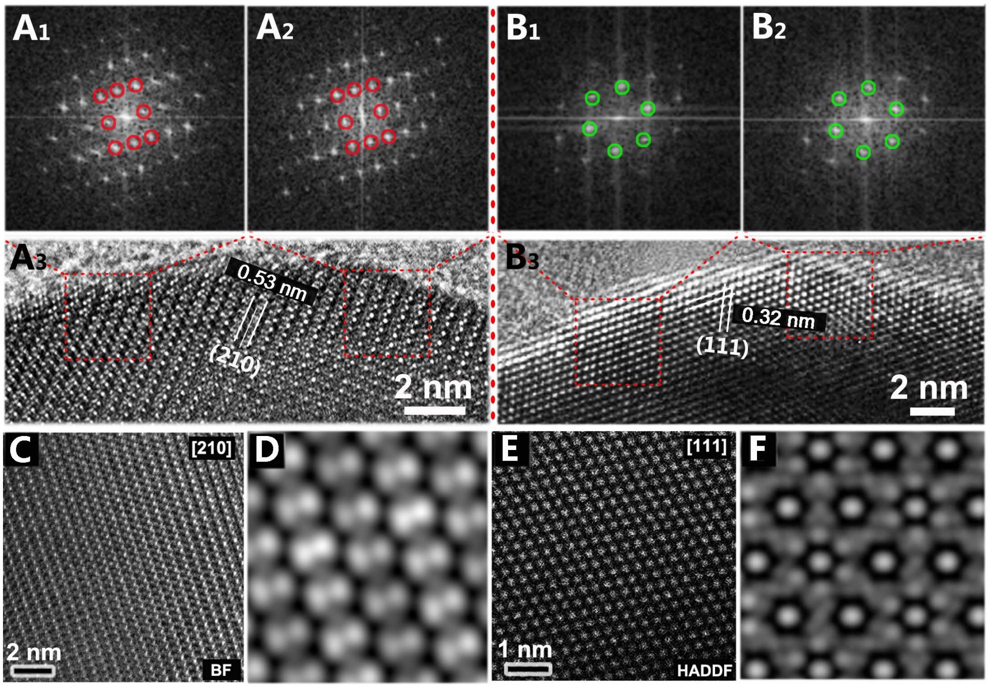

Figure 3. The corresponding FFT images of the exposed (210) ($A_{1,2,3}$) and (111) ($B_{1,2,3}$) facets for $Fe_5Co_4Ni_{20}Se_{36}B_x$ particle; (C, D) and (E, F) HRTEM and simulated images of $Fe_5Co_4Ni_{20}Se_{36}B_x$ with the three typical zone axis [210], [111].

In order to characterize the chemical states of the synthesized $Fe_5Co_4Ni_{20}Se_{36}B_x$ materials, we perform X-ray photoelectron spectroscopy (XPS). Figure 4A-E clearly show the Fe, Co, Ni, Se and B signals in the XPS spectrum. Obviously, the elements of Fe, Co, Ni mainly exist as oxidation states in the $Fe_5Co_4Ni_{20}Se_{36}B_x$ materials. For Fe 2p spectrum, the multiple peaks at 711.79, 715.26, 725.49 and 729.35 eV are assigned to Fe-B, Fe^{3+} $2p_{3/2}$, Fe^{2+} $2p_{1/2}$ and Fe^{3+} $2p_{1/2}$, respectively, along with the corresponding satellite peaks at 720.19 and 734.01 eV.[12,15] The $2p_{3/2}$ peaks of Co 2p spectrum (Figure 4B) can be decomposed into three peaks at 776.39, 781.68, and 786.75 eV, which are associated with Co-B, Co^{2+} and a satellite peak.[11] Similarly, the Ni $2p_{3/2}$ peaks can be assigned to Ni-B, Ni^{2+}, Ni^{3+} and satellite peak at 851.6 eV, 856.2 eV, 859.9 eV and 862.7 eV.[11,14] The corresponding XPS spectra of Fe, Co, Ni indicate that the electrons are transferred from these transitional metals into boron atoms in the $Fe_5Co_4Ni_{20}Se_{36}B_x$ materials. The B1s spectrum clearly shows two chemical forms, including M-B (M=Fe, Co, Ni) (185.68 eV) and trivalent oxidation states (192.15 eV).[11] The surface oxidation stems from the inevitably direct exposure to the ambient environment. The Se 3d XPS spectrum is fitted into two peaks at 54.74 (Se $3d_{5/2}$) and 55.73 eV (Se $3d_{3/2}$), which originate from the Se^{2-} of $Fe_5Co_4Ni_{20}Se_{36}B_x$.[7,17] In addition, a doublet peak (58.8 eV) assigned to the oxidation state of Se species can be attributed to the oxidation of Se at $Fe_5Co_4Ni_{20}Se_{36}B_x$ surface.[7,17] The XPS spectra of $NiSe_x$, B-$NiSe_x$ and Ni2p in Figure S4 further reveal that electron transfer from transitional metals into B atoms. Through density function theory (DFT) calculations, we also found that the B atoms are bonded with surrounding atoms, which can be demonstrated by projected density of states (PDOS) of atoms in $Fe_{0.125}Co_{0.125}Ni_{0.75}Se_2B_{0.2}$, as displayed in Figure 4F. Clearly, the *p* orbital of B (red line) is overlapped with outermost orbital of other atoms around B, including *p* orbital of Se and *d* orbital of metal atoms. To accurately describe the bonding state of B to metal atoms, the negative Crystal Orbital Hamilton Population (-COHP) between B and metals are calculated by Lobster code[39], which can describe detailed chemical interactions of bonding states between two atoms, as well as their bond states of orbital (Figure S5). The positive –COHP values represent the bonding state, and the negative values represent the anti-bonding. Clearly, the –COHP curves below the Femi level almost lie in the region of positive values, which means that the B *2p* orbitals are bonded with *3d* orbitals of metals, and some of electrons between B-Metals are easy to lose for the existence of negative values under Fermi level, which is beneficial for the catalysis processes. These results suggest that B atoms bond with surrounding atoms, which is consisted with our experimental results (Figure 4A-E).

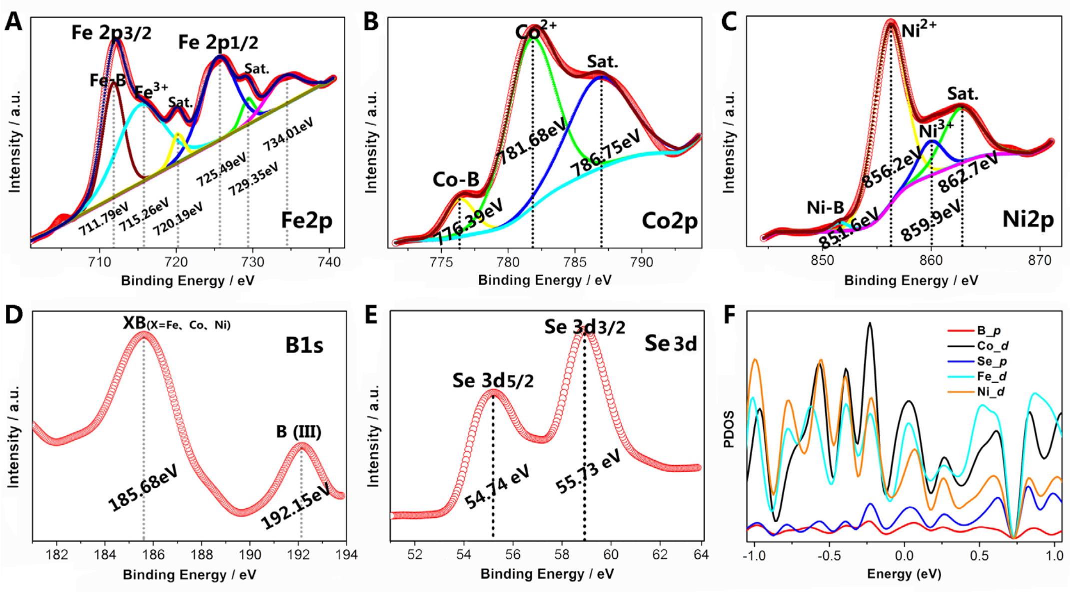

Figure 4. (A-E) X-ray photoelectron spectroscopy (XPS) spectra for the $Fe_5Co_4Ni_{20}Se_{36}B_x$ MMC, (F) Projected density of states (PDOS) of $Fe_{0.125}Co_{0.125}Ni_{0.75}Se_2B_{0.2}$.

The electrocatalytic OER activities of the prepared materials were investigated using a standard three-electrode half-cell and 1.0 M KOH as the electrolyte. The NiSeB, FeNiSeB and CoNiSeB compounds were adopted as the control samples to understand the activity of the $Fe_5Co_4Ni_{20}Se_{36}B_x$ composite. The SEM images and the corresponding EDS analysis of the $NiSe_2B_x$, $FeNi_3Se_8B_x$ and $CoNi_3Se_8B_x$ (Figure S6-8) show their similar structure with stable element composition. Based on the OER polarization curves (Figure 5A), the $Fe_5Co_4Ni_{20}Se_{36}B_x$ composite obviously exhibits the lowest overpotential (η) of 279.8 mV to reach a current density of 10 mA cm^{-2}, compared to those of $NiSe_2B_x$, $FeNi_3Se_8B_x$ and $CoNi_3Se_8B_x$ (543, 335, and 453 mV, respectively. The current density at η = 250 mV is 7.3 mA cm^{-2}, which is 4.6-, 4.4- and 3.8-fold higher than those of $NiSe_2B_x$, $CoNi_3Se_8B_x$, and $FeNi_3Se_8B_x$, respectively (Figure S9). The Tafel slopes of these catalysts were further investigated to estimate their OER performance. As presented in Fig. 5B, the Tafel slopes are 59.5, 86.3, 121, and 161 mV dec^{-1} for $Fe_5Co_4Ni_{20}Se_{36}B_x$, $FeNi_3Se_8B_x$, $CoNi_3Se_8B_x$, and $NiSe_2B_x$, respectively. The $Fe_5Co_4Ni_{20}Se_{36}B_x$ MMC exhibited the smallest Tafel slope, which suggests more favorable OER kinetics than the other samples. The electrochemically active surface areas (ESCAs) of these catalysts were evaluated from the double-layer capacitance (Cdl) (Figure S10). The ECSA-normalized polarization curves presented in Figure S11 show that current densities of $Fe_5Co_4Ni_{20}Se_{36}B_x$ is still higher than those of other three catalysts. The OER kinetics of these catalysts were further investigated by electrochemical impendence spectroscopy (Figure S12), exhibiting similar results. This outstanding OER performance of $Fe_5Co_4Ni_{20}Se_{36}B_x$ is superior compared to most of the other selenides or Fe/Co/Ni-based OER catalysts in alkaline solution, as well as the noble metal oxides IrO_x and RuO_2 (Figure 5C and Table S1, S2 in the Supporting Information). We investigate the effect of metal doping on the overpotential through DFT calculations. Figure 5D shows the overpotentials for the catalysts with and without B dopants. These results indicate that the catalysts with FeCo co-doping exhibit lower overpotentials than that with Fe or Co-doped surfaces. Meanwhile, the Fe or Co-doped surfaces without B also have higher overpotential than FeCo co-doping ones with B-doping. These results indicate that the co-doped metals atoms are also beneficial to OER processes, which is consistent with our experimental results.

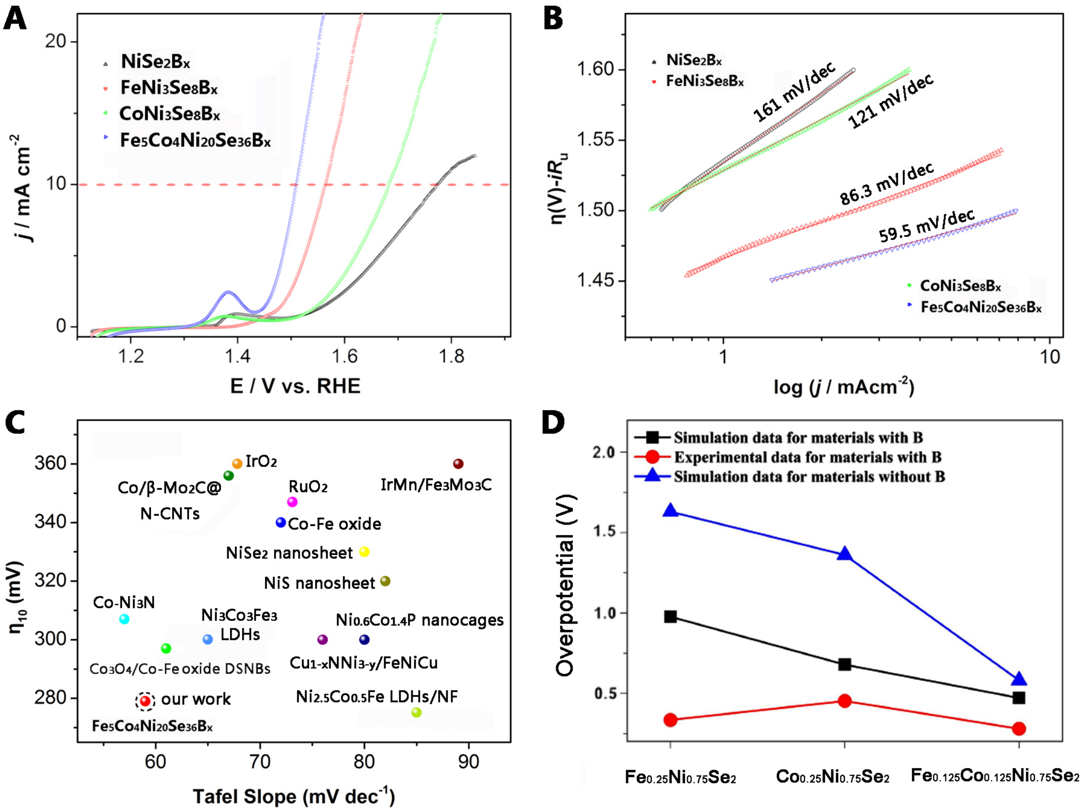

Figure 5. Electrochemical performances of $NiSe_2B_x$, $FeNi_3Se_8B_x$, $CoNi_3Se_8B_x$ and $Fe_5Co_4Ni_{20}Se_{36}B_x$ for OER. (A) iR-corrected polarization curves obtained in 1.0 M KOH at a scan rate of 2 mV s^{-1}; (B) The corresponding Tafel plots; (C) Tafel slopes and overpotentials of $Fe_5Co_4Ni_{20}Se_{36}B_x$ compared with other OER catalysts (Table S2). (D) The overpotentials from experimental and theoretical works.

Long-term stability of the catalysts is another critical factor for practical applications. As shown in Figure S13, the $Fe_5Co_4Ni_{20}Se_{36}B_x$ maintain a current density of 10 mA cm^{-2} over a period of at least 10 hours without obvious potential increase, suggesting the excellent durability of the synthesized $Fe_5Co_4Ni_{20}Se_{36}B_x$. Figure S14 shows the TEM image and the STEM elemental mapping images of the $Fe_5Co_4Ni_{20}Se_{36}B_x$ after the durability test, respectively. During the durability test, the $Fe_5Co_4Ni_{20}Se_{36}B_x$ particles were slightly enlarged (Figure S14A) on the amorphous membrane. The distribution of elements for $Fe_5Co_4Ni_{20}Se_{36}B_x$ after the stability test demonstrates the excellent structural durability of the multimetallic selenide-boride with maintaining stable elemental composition. The excellent stability is attributed to the presence of the support of homogeneous membrane, which prevents the agglomeration of catalytic nanoparticles as a result of the strong interaction by the *in situ* growth.

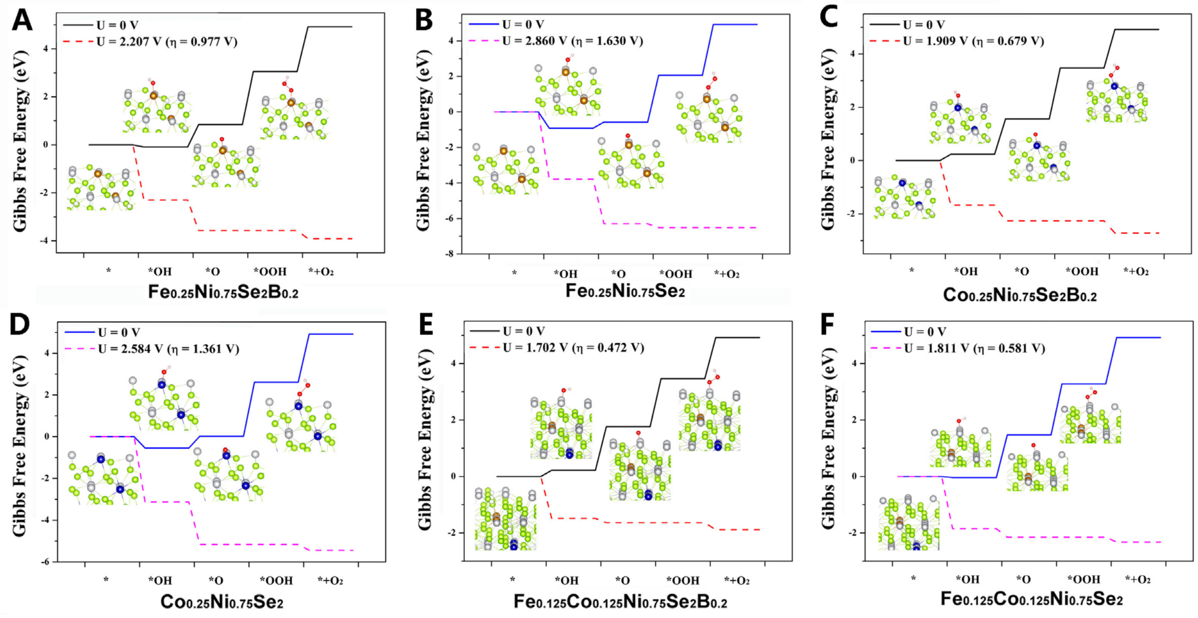

Figure 6. Activities of OER intermediate process for calculated with DFT+U. The processes of OER steps on (111) surfaces of different materials: (A) $Fe_{0.25}Ni_{0.75}Se_2$, (B) $Fe_{0.25}Ni_{0.75}Se_2B_{0.2}$, (C) $Co_{0.25}Ni_{0.75}Se_2$, (D) $Co_{0.25}Ni_{0.75}Se_2B_{0.2}$, (E) $Fe_{0.125}Co_{0.125}Ni_{0.75}Se_2$ and (F) $Fe_{0.125}Co_{0.125}Ni_{0.75}Se_2B_{0.2}$. The solid line: the computed free energies without external voltage (U=0), and the dashed line: the modified free energies under theoretical reaction potential.

To understand the effect of $Fe_5Co_4Ni_{20}Se_{36}B_x$ on the promotion of the activity of the oxygen evolving catalysts, we performed DFT calculations to evaluate the composition effect on the energetics of OER intermediates, including (111) surfaces of pristine structures and their corresponding ones with B dopants (namely, $Fe_{0.25}Ni_{0.75}Se_2$, $Fe_{0.25}Ni_{0.75}Se_2B_{0.2}$, $Co_{0.25}Ni_{0.75}Se_2$, $Co_{0.25}Ni_{0.75}Se_2B_{0.2}$, $Fe_{0.125}Co_{0.125}Ni_{0.75}Se_2$, $Fe_{0.125}Co_{0.125}Ni_{0.75}Se_2B_{0.2}$). Figure 6 shows the Gibbs free energy (ΔG) for each OER intermediate steps, where the solid line indicates the computed free energies without external voltage (U=0), and the dashed line represents the modified free energies under theoretical reaction potential. For $Fe_{0.25}Ni_{0.75}Se_2$ (Figure 5A), the overpotential value for OER is 1.63 V. This large overpotential is mainly limited by the high desorption ΔG of 2.86 eV for the step of $*OOH \rightarrow * + O_2 + H^+ + e$, where * represents the catalyst. In contrast, the B-doped $Fe_{0.25}Ni_{0.75}Se_2$ has lower but still large overpotential of 0.977 V, which can be attributed to the stronger adsorption to the OOH-based intermediate, (the corresponding ΔG for limit step is 2.207 eV). Details of relationship between overpotential value and ΔG is described in section of "Calculation methods". Similarly, the other catalysts with B dopants exhibit smaller overpotential than that of pristine ones. Specifically, the overpotentials of $Co_{0.25}Ni_{0.75}Se_2$, $Co_{0.25}Ni_{0.75}Se_2B_{0.2}$, $Fe_{0.125}Co_{0.125}Ni_{0.75}Se_2$, $Fe_{0.125}Co_{0.125}Ni_{0.75}Se_2B_{0.2}$ are 1.361 V, 0.679 V, 0.581 V and 0.472 V, respectively.

We also investigated the deformation charge density for all surfaces and the PDOS at active sites to understand the effects of multimetal and B-doping on the activity of the OER catalysts. Figure S15 shows the deformation charge density of selected (111) facets. For the catalysts with B dopants, electrons (yellow area in Figure S15) are clearly accumulated around B atom (white balls in Figure S15). These electrons are transferred from adjacent metals atoms, where the electron deletion areas (displayed as cyan area in Figure S15) are only located on metal atoms. Such polarized charge distribution strengthens the interaction between B and metal atoms, and reduces the number of electrons in metal atoms, especially the outermost electrons in *d* orbit, which heavily modifies the properties of metals sites. Taking $Co_{0.25}Ni_{0.75}Se_2$ (Figure 6C) and $Co_{0.25}Ni_{0.75}Se_2B_{0.2}$ (Figure 6D) as the examples, the strong adsorption of -OOH group limits the overpotential of $Co_{0.25}Ni_{0.75}Se_2$. The Gibbs free energy difference (ΔG) for the generation of OOH-based intermedium (*OOH) is 2.584 eV, which is greatly reduced to 1.909 eV with the B dopants (Figure 6C). This reduction can be understood as a result of the loss of *d* electrons of metal atoms, as displayed in Figure S15, which reduces the possibility of the charge transfer from metal atoms to –OOH group and gives rise to a weak interaction between metal site and –OOH group. As a result, the Gibbs energy ΔG is reduced for the OER process. Through Bader analyzing,[40] the total electrons of –OOH group on $Co_{0.25}Ni_{0.75}Se_2B_{0.2}$ is 13.489e, which means that –OOH group accepts 0.489e from

$Co_{0.25}Ni_{0.75}Se_2B_{0.2}$. In contrast, the electrons transferred from $Co_{0.25}Ni_{0.75}Se_2$ to –OOH group is 0.527e. The proposed OER mechanisms for selenides before and after B dopant shown in Figure 7A, B clearly show that the B dopant weakens the interaction between catalyst and –OOH group as the results of ΔG. Similar phenomena are also observed for other multimetllic selenide-borides. Figure 7C shows the PDOS of *d* orbitals of atoms at active sites, indicating that the *d* electron of metal atoms are redistributed with the introduction of other metal atoms and B. We also calculated the number of *d* electrons of active metal sites. The B-doping can reduce the total *d* electrons around metals, which have been transferred to B atoms, consisted with the data of deformation charge density. In addition, the transfer of *d* electrons from metals to B enhances the interactions between B and metals, which can reasonably explain the present of M-B bonds in XPS data in Figure 4.

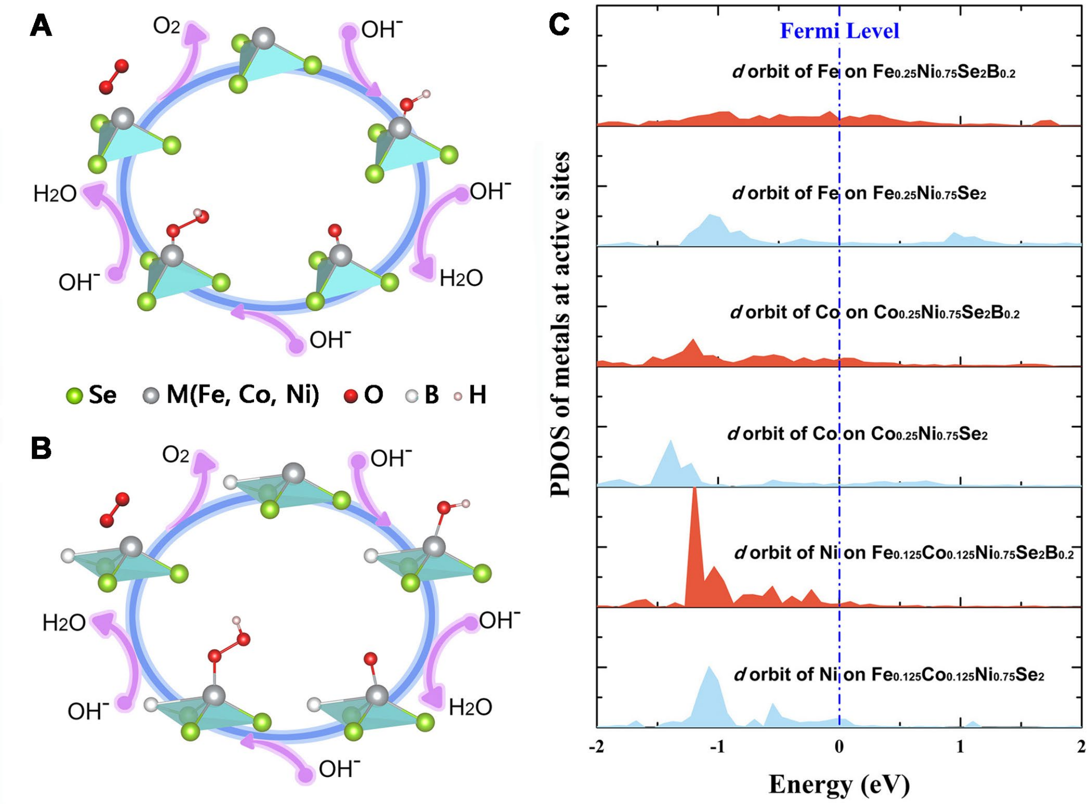

Figure 7. (A, B) Proposed OER mechanisms for pyrite selenides before and after B dopant; (C) PDOS of atoms at active sites.

CONCLUSIONS

In summary, the heteroepitaxial pyrite selenides by dual-cation substitution and boron dopant can effectively prevent corrosion benefiting from the *in situ* nucleation growth process, and exhibit superior OER activity and stability. In particular, boron in the $Fe_5Co_4Ni_{20}Se_{36}B_x$ can effectively adjust the adsorption energy of OH intermediates, and facilitates the charge transfer from the surface to current collector. The synergistic effect between the embedded B, Se and Fe, Co, Ni in the pyrite selenides can generate active sites that further improve the OER reaction kinetics. This work illustrate the potential of multimetallic selenide-boride materials in energy conversion owing to the special atomic and electronic structures, which may contribute to rationally fabricating high performance electrocatalysts.

EXPERIMENTAL METHODS

Materials synthesis. The $NiSe_2B_x$, $FeNi_3Se_8B_x$, $CoNi_3Se_8B_x$ and $Fe_5Co_4Ni_{20}Se_{36}B_x$ powders were synthesized by two simple steps. Firstly, the Ni, FeNi, CoNi, and FeCoNi based precursors were synthesized by chemical methods. 1mmol $Co(NO_3)_2{\cdot}6H_2O$ (Sigma-Aldrich), 1mmol $Ni(NO_3)_2{\cdot}6H_2O$ (Sigma-Aldrich), and 1mmol $FeCl_3{\cdot}6H_2O$ (Sigma-Aldrich) were dissolved in DI water to form a transparent solution, respectively. The FeCoNi based precursor was prepared by adding moderate $NaBH_4$ (Sigma-Aldrich) solution into the $Ni(NO_3)_2{\cdot}6H_2O$ (1mmol), $Co(NO_3)_2{\cdot}6H_2O$ and $FeCl_3{\cdot}6H_2O$ (1mmol) mixed solution (Mole ratio of 3:0.5:0.5), then a black precipitate was immediately produced. The precipitate was collected and dried at 60 °C in an oven overnight. Then a thermal selenization process was employed in the following step to obtain the $Fe_5Co_4Ni_{20}Se_{36}B_x$. The as-prepared precipitate and selenium powder were placed in a quartz boat. The selenium powder (Alfa Aesar) was put at the upstream side of the tube furnace with a distance of 10 cm to the precipitate. Subsequently, the precipitate was heated at 450 °C for 2 h with a heating rate of 5 °C min^{-1} under argon atmosphere, and finally cooled to ambient temperature naturally. For comparison,

$NiSe_2B_x$, $FeNi_3Se_8B_x$, $CoNi_3Se_8B_x$ were also prepared under the similar conditions despite the differences of metal irons.

Structural characterizations. Powder XRD data were obtained through an X-ray diffractometer (Rigaku SmartLab) using Cu Kα (γ=1.54178 A) radiation. SEM images were recorded in a field-emission scanning electron microscope (JSM-6490, JEOL) operating at 5 kV. TEM and HRTEM, selected area electron diffraction (SAED), and electron energy loss spectroscopy (EELS) energy-dispersive X-ray spectroscopy (EDX) elemental mapping were collected on a JEOL model JEM-ARM-200F microscope operated at 200 kV. X-ray photoelectron spectroscopy (XPS) was acquired on an ESCALAB 250Xi XPS system using Mg as the excitation source.

Electrochemical measurements. To prepare the working electrode, 5 mg catalysts were dispersed in 750 μL of DI water, 210 μL of isopropanol and 40 μL of 5 wt% Nafion solution followed by sonication to form a homogeneous ink. Then 10 μL of the ink was loaded onto a glassy carbon electrode of 5 mm in diameter. Then the electrode was dried naturally at room temperature. Electrochemical measurements were carried out on a CHI 660E electrochemical workstation (CH Instruments, Inc., Shanghai) in a standard three-electrode system at room temperature with an aqueous solution of 1.0 M KOH (PH = 14) used as the electrolyte. A Hg/HgO (1.0 M NaOH) electrode and a graphite rod were used as the reference electrode and counter electrode, respectively. All the measured potentials vs Hg/HgO were converted to reversible hydrogen electrode according to the equation: E(RHE) = E(Hg/HgO) + 0.098 + 0.059 pH. The polarization curves obtained from linear sweep voltammetry (LSV) measurements were recorded at a scan rate of 1.0 mV s^{-1}. Electrochemical impendence spectroscopy (EIS) measurements were performed in Solartron Electrochemical workstation (German) in the frequency ranging from 0.01 to 105 Hz with small AC voltage amplitude, of which the data were fitted by Zview software. The electrochemically active surface area

(ECSA) was determined by the electrochemical double-layer capacitance (Cdl) from the scan-rate dependence of CVs.

Calculation methods. Vienna *Ab Initio* Simulation Package (VASP) code were employed to study the adsorption of OH groups on the potential catalysts.[41] The nuclei–electron interactions were described by the projector augmented wave (PAW) pseudo-potentials,[42] at the level of generalized gradient approximation (GGA) in the form of Perdew, Burke, and Ernzerhof (PBE).[43] The spin-polarization was considered in these calculations, as well as the van der Waals interaction, which was described by DFT+D3 method developed by Grimme.[44,45] Further, the Coulombic interaction for transition metals are corrected by GGA + U approach, in which the parameters of Ueff of 3.4 eV, 3.4 eV and 3.3 eV were used for Ni, Co and Fe, respectively. For all calculations, the cut off energy was 500 eV, and the convergence criterions are 10^{-5} eV for energy and 10^{-2} eV/Å for force. Methods for the process of OER were in more details described in our initial previous work.[46]

ASSOCIATED CONTENT

Supporting Information

The Supporting Information is available free of charge on the ACS Publications website.

The following files are available free of charge.

Figures S1−S11 and Tables S1−S2 (PDF)

AUTHOR INFORMATION

Corresponding Author

*E-mail: ychai@polyu.edu.hk

Author Contributions

Y. Z., D. R., S. M.contributed equally. Notes The authors declare no competing financial interest. ACKNOWLEDGMENTS This work was supported by the Research Grant Council of Hong Kong (N_PolyU540/17), the Hong Kong Polytechnic University (G-YBPS), the Scientific and Technological Projects of Henan Province (182102210502), and Education Department of Henan Province (18A430003), the National Natural Science Foundation of China (No. 51801075, 91750112). The calculation work was carried out at National Supercomputer Center in LvLiang of China, and the calculations were performed on TianHe-2.

REFERENCES

(1) Suen N., Hung S., Quan Q., Zhang N., Xu Y. and Chen H. Electrocatalysis for the Oxygen Evolution Reaction: Recent Development and Future Perspectives. *Chem. Soc. Rev.* **2017**, 46, 337–365.

(2) Yao Y., Huang Z., Xie P., Lacey S. D., Jacob R., Xie H., Chen F., Nie A., Pu T., Rehwoldt M., *et al.* Carbothermal Shock Synthesis of High-Entropy-Alloy Nanoparticles. *Science* **2018**, 359, 1489–1494.

(3) Chu S. and Majumdar A. Opportunities and Challenges for a Sustainable Energy Future. *Nature* **2012***,* 488, 294–303.

(4) Zhang B., Zheng X., Voznyy O., Comin R., Bajdich M., García-Melchor M., Han L., Xu J., Liu M., Zheng L., *et al.* Homogeneously Dispersed Multimetal Oxygen-Evolving Catalysts. *Science* **2016***,* 352, 333–337.

(5) Hu F., Zhu S., Chen S., Li Y., Ma L., Wu T., Zhang Y., Wang C., Liu C., Yang X., *et al.* Amorphous Metallic NiFeP: A Conductive Bulk Material Achieving High Activity for Oxygen Evolution Reaction in Both Alkaline and Acidic Media. *Adv. Mater.* **2017**, 29, 1606570.

(6) McCrory C., Jung S., Peters J. and Jaramillo T. F. Benchmarking Heterogeneous Electrocatalysts for the Oxygen Evolution Reaction. *J. Am. Chem. Soc.* **2013**, 135, 16977−16987.

(7) Anantharaj V., Ede S. R., Sakthikumar K., Karthick K., Mishra S., and Kundu S. Recent Trends and Perspectives in Electrochemical Water Splitting with an Emphasis on Sulfifide, Selenide, and Phosphide Catalysts of Fe, Co, and Ni: A review. *ACS Catal.* **2016***,* 6, 8069−8097.

(8) Friebel D., Louie M., Bajdich M., Sanwald K., Cai Y., Wise A., Cheng M., Sokaras D., Weng T., Alonso-Mori R., *et al*. Identification of Highly Active Fe Sites in (Ni, Fe)OOH for Electrocatalytic Water Splitting. *J. Am. Chem. Soc*. **2015**, 137, 1305−1313.

(9) Mendoza-Garcia A., Zhu H., Yu Y., Li Q., Zhou L., Su D., Kramer M. J., Sun S., Controlled Anisotropic Growth of Co-Fe-P from Co-Fe-O Nanoparticles. *Angew. Chem. Int. Ed.* **2015**, 54, 9642.

(10) Xia C., Jiang Q., Zhao C., Hedhili M. N., Alshareef H. N., Selenide-based Electrocatalysts and Scaffolds for Water Oxidation Applications. *Adv. Mater.* **2016**, 28, 77–85.

(11) Kim J., Kim B., Kim H., and Kang K., Recent Progress on Multimetal Oxide Catalysts for the Oxygen Evolution Reaction. *Adv. Energy Mater.* **2018***,* 8, 1702774.

(12) Qiu B., Cai L., Wang Y., Lin Z., Zuo Y., Wang M., and Chai Y. Fabrication of Nickel–Cobalt Bimetal Phosphide Nanocages for Enhanced Oxygen Evolution Catalysis. *Adv. Funct. Mater.* **2018**, 28, 1706008.

(13) Liu Z., Dong C., Huang Y., Cen J., Yang H., Chen X., Tong X., Su D., Wang Y. and Wang S. Modulating the Electronic Structure of Ultrathin Layered Double Hydroxide Nanosheets with Fluorine: An Efficient Electrocatalyst for the Oxygen Evolution Reaction. *J. Mater. Chem. A* **2019**, 7, 14483-14488.

(14) Zhou P., He J., Zou Y., Wang Y., Xie C., Chen R., Zang S. & Wang S. Single-Crystalline Layered Double Hydroxides with Rich Defects and Hierarchical Structure by Mild

Reduction for Enhancing the Oxygen Evolution Reaction. *Sci. China Chem.* **2019**, 62, https://doi.org/10.1007/s11426-019-9511-x.

(15) Jiang J., Sun F., Zhou S., Hu W., Zhang H., Dong J., Jiang Z., Zhao J., Li J., Yan W., Wang M. Atomic-Level Insight into Super-Efficient Electrocatalytic Oxygen Evolution on Iron and Vanadium co-Doped Nickel (oxy)Hydroxide. *Nat. Commun*. **2018**, 9, 2885.

(16) Liu G., He D., Yao R., Zhao Y., and Li J., Amorphous NiFeB Nanoparticles Realizing Highly Active and Stable Oxygen Evolving Reaction for Water Splitting. *Nano Res.* **2018**, 3, 1664–1675.

(17) Zuo Y., Rao D., Li S., Li T., Zhu G., Chen S., Song L., Chai Y., Han H. Atomic Vacancies Control of Pd-Based Catalysts for Enhanced Electrochemical Performance. *Adv. Mater*. **2018**, 30, 1704171.

(18) Xu K., Chen P. Z., Li X., Tong Y., Ding H., Wu X., Chu W., Peng Z., Wu C., Xie Y. Metallic Nickel Nitride Nanosheets Realizing Enhanced Electrochemical Water Oxidation. *J. Am. Chem. Soc.* **2015***,* 137, 4119–4125.

(19) Bediako D. K., Surendranath Y., Nocera D. G., Mechanistic Studies of the Oxygen Evolution Reaction Mediated by a Nickel-Borate Thin Film Electrocatalyst. *J. Am. Chem. Soc.* **2013**, 135, 3662–3674.

(20) Masa J., Weide P., Peeters D., Sinev I., Xia W., Sun Z., Somsen C., Muhler M., Schuhmann W. Amorphous Cobalt Boride (Co_2B) as A Highly Efficient Nonprecious Catalyst for Electrochemical Water Splitting: Oxygen and Hydrogen Evolution. *Adv. Energy Mater.* **2016**, 6, 1502313.

(21) Chen P. , Xu K., Zhou T., Tong Y., Wu J., Cheng H., Lu X., Ding H., Wu C., Xie Y. Strong-Coupled Cobalt Borate Nanosheets/graphene Hybrid as Electrocatalyst for Water Oxidation Under Both Alkaline and Neutral Conditions. *Angew. Chem. Int. Ed.* **2016**, 55, 2488–2492.

(22) Zuo Y., Li T., Ren H., Zhu G., Han K., Zhuang L. and Han H. Self-Assembly of Pt-based Truncated Octahedral Crystals into Metal-Frameworks Towards Enhanced Electrocatalytic Activity. *J. Mater. Chem. A* **2016**, 4, 15169–15180.

(23) Mistry H., Varela A., Kühl S., Strasser P., Cuenya B. R. Nanostructured Electrocatalysts with Tunable Activity and Selectivity. *Nat. Rev. Mater.* **2016***,* 1, 1–14.

(24) Zuo Y., Wu L., Cai K., Li T., Yin W., Li D., Li N., Liu J. and Han H. Platinum Dendritic-Flowers Prepared by Tellurium Nanowires Exhibit High Electrocatalytic Activity for Glycerol Oxidation. *ACS Appl. Mater. Interfaces* **2015**, 7, 17725−17730.

(25) Xiang X., Fang S., Hu X. A Nickel Iron Diselenide-Derived Efficient Oxygen-Evolution Catalyst. *Nat. Commun*. **2016**, 7, 12324.

(26) Sun Y., Xu K., Wei Z., Li H., Zhang T., Li X., Cai W., Ma J., Fan H., and Li Y. Strong Electronic Interaction in Dual-Cation-Incorporated $NiSe_2$ Nanosheets with Lattice Distortion for Highly Efficient Overall Water Splitting. *Adv. Mater.* **2018**, 30, 1802121.

(27) Tang C., Zhang R., Lu W., He L., Jiang X., Asiri A. M., Sun X. Fe-Doped CoP Nanoarray: A Monolithic Multifunctional Catalyst for Highly Efficient Hydrogen Generation. *Adv. Mater.* **2017**, 29, 1602441.

(28) Han H., Choi H., Mhin S., Hong Y., Kim K., Kwon J., Ali G., Chung K., Je M., Umh H., *et al*. Advantageous Crystalline-Amorphous Phase Boundary for Enhanced Electrochemical Water Oxidation. *Energy Environ. Sci.* **2019**, 12, 2443-2454.

(29) Jiang J., Lu S., Gao H., Zhang X., Yu H. Ternary $FeNiS_2$ Ultrathin Nanosheets as An Electrocatalyst for Both Oxygen Evolution and Reduction Reactions. *Nano Energy* **2016**, 27, 526-534.

(30) Gao S., Lin Y., Jiao X., Sun Y., Luo Q., Zhang W., Li D., Yang J., Xie Y. Partially Oxidized Atomic Cobalt Layers for Carbon Dioxide Electroreduction to Liquid Fuel, *Nature* **2016**, 529, 68.

(31) Chen C., Kang Y., Huo Z., Zhu Z., Huang W., Xin H., Snyder J., Li D., Herron J., Mavrikakis M., *et al.* Highly Crystalline Multimetallic Nanoframes with Three-Dimensional Electrocatalytic Surfaces. *Science* **2014**, 343, 1339.

(32) George C., Genovese A., Casu A., Prato M., Povia M., Manna L., and Montanari T. CO Oxidation on Colloidal $Au_{0.8}Pd_{0.2}$–Fe_xO_y Dumbbell Nanocrystals. *Nano Lett.* **2013**, 13, 752–757.

(33) Cortie M. B. and McDonagh A. M. Synthesis and Optical Properties of Hybrid and Alloy Plasmonic Nanoparticles. *Chem. Rev.* **2011**, 111, 3713–3735.

(34) McCrory C., Jung S., Peters J. C., and Jaramillo T. F. Benchmarking Heterogeneous Electrocatalysts for the Oxygen Evolution Reaction. *J. Am. Chem. Soc*. **2013**, 135, 16977-16987.

(35) Tung C., Hsu Y., Shen Y., Zheng Y., Chan T., Sheu H., Cheng Y., Chen H. Reversible Adapting Layer Produces Robust Single-Crystal Electrocatalyst for Oxygen Evolution. *Nat. Commun.* **2015**, 6, 8106.

(36) Liang H., Meng F., Cabán-Acevedo M., Li L., Forticaux A., Xiu L., Wang Z., and Jin S. Hydrothermal Continuous Flow Synthesis and Exfoliation of NiCo Layered Double Hydroxide Nanosheets for Enhanced Oxygen Evolution Catalysis. *Nano Lett.* **2015***,* 15, 1421.

(37) Lin C., Tsai Y., Johnston H. E., Fang M., Yu F., Zhou W., Whitfifield P., Li Y., Wang J., Liu R., *et al.* Enhanced Photoluminescence Emission and Thermal Stability from Introduced Cation Disorder in Phosphors. *J. Am. Chem. Soc*. **2017**, 139, 11766−11770.

(38) Wang B., Lin H., Huang F., Xu J., Chen H., Lin Z., and Wang Y. Non-rare-earth $BaMgAl_{10-2x}O_{17}$:xMn^{4+}, xMg^{2+}: A Narrow-Band Red Phosphor for Use as A High-Power Warm w-LED. *Chem. Mater.* **2016**, 28, 3515−3524.

(39) Maintz S., Deringer V., Tchougréeff A., Dronskowski R. LOBSTER 2.0.0 and its Nuts and Bolts. *J. Comput. Chem*. **2016**, 37, 1030 – 1035.

(40) Yu M. and Trinkle D. R. Accurate and Efficient Algorithm for Bader Charge Integration. *J. Chem. Phys.* **2011**, 134, 064111.

(41) Kresse G., Furthmuller J. Efficient Iterative Schemes for *Ab Initio* Total-energy Calculations Using A Plane-wave Basis Set. *Phys. Rev. B* **1996**, 54, 11169-11186.

(42) Kresse G., Furthmüller J. Efficiency of *Ab Initio* Total Energy Calculations for Metals and Semiconductors Using a Plane-wave Basis Set. *Comput. Mater. Sci*. **1996**, 6, 15-50.

(43) Blöchl P. E. Projector Augmented-Wave Method. *Phys. Rev. B* **1994**, 50, 17953-17979.

(44) Perdew J. P., Burke K., Ernzerhof M. Generalized Gradient Approximation Made Simple. *Phys. Rev. Lett.* **1996**, 77, 3865-3868.

(45) Grimme S., Antony J., Ehrlich S., and Krieg S. A Consistent and Accurate *Ab Initio* Parametrization of Density Functional Dispersion Correction (DFT-D) for the 94 Elements H-Pu. *J. Chem. Phys.* **2010**, 132, 154104.

(46) Meng L., Rao D., Tian W., Cao F., Yan X., Li L. Simultaneous Manipulation of O-Doping and Metal Vacancy in Atomically Thin $Zn_{10}In_{16}S_{34}$ Nanosheet Arrays toward Improved Photoelectrochemical Performance. *Angew. Chem. Int. Ed.* **2018**, 130, 17124–17129.

TOC

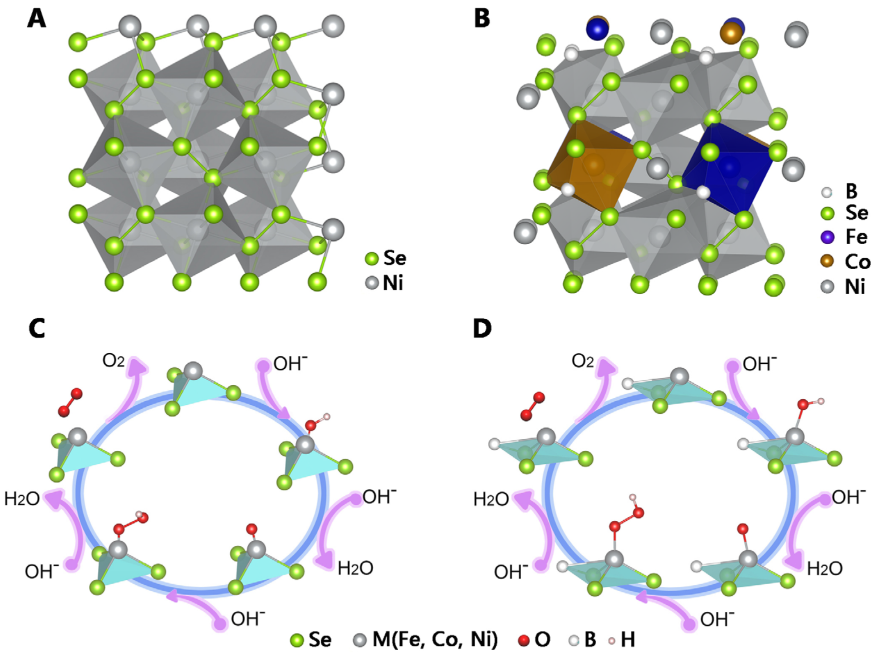
A
Se
Ni
B
B
Se
Fe
Co
Ni
C
O2
OH⁻
H2O
OH⁻
OH⁻
H2O
OH⁻
D
O2
OH⁻
H2O
OH⁻
OH⁻
H2O
OH⁻
Se
M(Fe, Co, Ni)
O
B
H